NANO LETTERS

pubs.acs.org/NanoLett Letter

# All-Solution-Processed Sky-Blue Perovskite Electroluminescence Device via Integrated Supramolecular Host–Guest Post-Treatment

Naizhong Jiang, Zhibin Wang,* Song Zheng, Zhehong Zhou, Ruidan Zhang, Lingwei Zeng, Feng Huang, and Daqin Chen*

Cite This: https://doi.org/10.1021/acs.nanolett.5c06313 Read Online

ACCESS | Metrics & More | Article Recommendations | Supporting Information

**ABSTRACT:** All-solution-processed perovskite optoelectronic devices are promising for scalable, sustainable manufacturing, yet their performance remains inferior to vacuum-deposited counterparts because solvents used for subsequent charge transport layers often damage the underlying emissive layer. Herein, we find that when fabricating the electron transport layer (ETL) on sky-blue quasi-2D perovskite films using solution processing, even nonpolar solvents degrade luminescence properties and surface morphology, primarily due to the loss of organic ligands and additives. To overcome this challenge, we develop a supramolecular host–guest complexation strategy that predissolves these organic components in nonpolar solvents and incorporates them directly into the ETL processing sequence. Using this method, we achieve a sky-blue PeLED with an external quantum efficiency of 14.75% and a maximum luminance of 8740 cd $m^{-2}$. This work provides a versatile and promising route to high-performance, all-solution-processed PeLEDs.

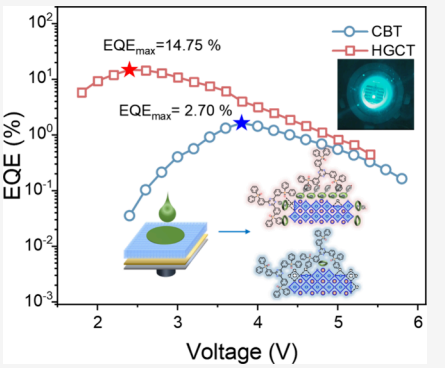


**KEYWORDS:** *perovskite, light-emitting diodes, all-solution-processed method, host–guest complex, post-treatment*



Metal halide perovskites have emerged as promising candidates for next-generation optoelectronic technologies, owing to their exceptional photoelectric properties, including wide color gamut, high photoluminescence quantum yield (PLQY), tunable bandgap, and narrow emission full-width at half-maximum (fwhm).[1−5] Since the first demonstration of high-performance perovskite light-emitting diodes (PeLEDs) at room temperature in 2014, the external quantum efficiencies (EQE) of red, green, and blue devices have advanced significantly, reaching 26%, 32%, and 30%, respectively.[6−9] These high-efficiency devices predominantly rely on electron transport layers (ETLs) fabricated via vacuum evaporation, a technique capable of producing pinhole-free, dense small-molecule multilayer structures.[9,10] However, the high equipment costs, complex and time-consuming processes, and low material utilization associated with vacuum evaporation hinder its commercial scalability for mass production of PeLEDs.[11−16] In contrast, all-solution-processed methods—such as spin-coating, blade-coating, spray-coating, and inkjet printing—enable the simultaneous deposition of perovskite and adjacent charge transport layers, offering a viable pathway toward low-cost, large-area, and scalable manufacturing. Consequently, developing an all-solution-processed method has become an urgent requirement for advancing the commercialization of PeLEDs.

Although all-solution-processed method offers potential advantages over conventional vacuum deposition for fabricating PeLEDs, several critical challenges remain in practical applications. The emissive layer is highly susceptible to redissolution during the subsequent deposition of charge transport layers if inappropriate solvents are used, leading to severe photoluminescence (PL) quenching and degraded device efficiency.[17,18] To minimize interfacial damage, nonpolar solvents such as hydrofluoroethers,[19,20] chlorobenzene (CB), or CB/dichloromethane mixtures are typically employed.[21] Alternatively, for perovskite quantum dot-based emissive layers, solvent resistance can be enhanced through ligand engineering.[22] Another approach involves incorporating organic ligands into the processing solvents to mitigate perovskite degradation. For example, Tian et al. incorporated phenethylammonium bromide into the ZnO nanocrystal ETL; the bromide ions passivated oxygen vacancies in the ZnO and simultaneously healed surface defects in the perovskite, thereby mitigating the detrimental effects of the ethanol-based solution on the perovskite film.[23]

However, achieving high-performance electroluminescence from blue quasi-two-dimensional (quasi-2D) perovskites remains challenging. Their distinct structure, characterized by small grains surrounded by bulky cations and organic additives,

Received: December 16, 2025
Revised: January 26, 2026
Accepted: February 6, 2026




https://doi.org/10.1021/acs.nanolett.5c06313
Nano Lett. XXXX, XXX, XXX−XXX

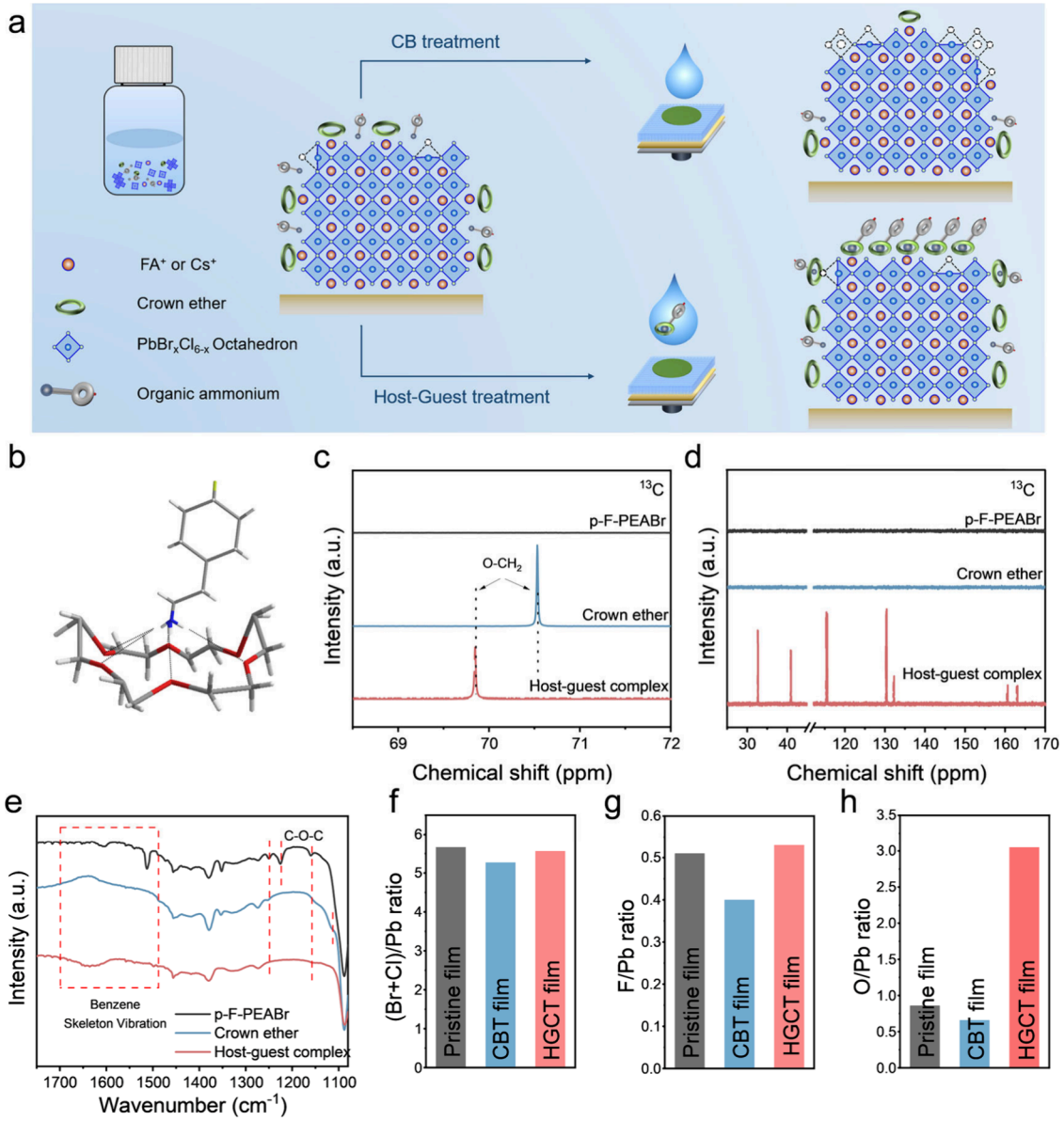


**Figure 1.** Host–guest complexation strategy for modulating perovskite film composition. a) Schematic illustration of the film processing and surface functionalization. b) Molecular structure of the designed host–guest complex formed between the crown ether and p-F-PEABr. c–d) $^{13}C$ NMR spectra and e) FTIR spectra of p-F-PEABr, the crown ether, and their host–guest complex. Statistical f) (Br+Cl)/Pb, g) F/Pb, and h) O/Pb atomic ratios of the pristine film, CB-treated (CBT) film, and host–guest complex-treated ("HGCT") film.

renders them incompatible with extra-situ ligand engineering techniques that are effective for quantum dots. Furthermore, unlike robust three-dimensional (3D) perovskite polycrystalline films, they lack inherent tolerance to nonpolar solvents.[24] Consequently, the luminescence properties of blue quasi-2D perovskites are highly susceptible to degradation during the solution deposition of charge transport layers, posing a significant obstacle for all-solution-processed PeLEDs.

Herein, we introduce a supramolecular strategy based on host–guest complexation between crown ether and ammonium salt molecules. This interaction enables their codissolution in nonpolar solvent, effectively preventing the solvent-induced dissolution of underlying quasi-2D perovskite layers—a primary cause of luminescence degradation during solution processing. This nonpolar solvent system is inherently compatible with small-molecule ETLs, allowing the integration of the ammonium salt passivation agent and the ETL material into a single ink. Consequently, a one-step spin-coating process simultaneously achieves perovskite surface reconstruction and ETL deposition. As a result, perovskite films treated with this host–guest strategy exhibit significantly lower nonradiative recombination losses than those processed with CB alone, indicating effective defect passivation and improved charge transport. The resulting optimized devices achieve a maximum luminance of 8740 cd $m^{-2}$ and an EQE of 14.75%, representing one of the highest performances reported for all-solution-processed blue PeLEDs.

Figure 1a illustrates the integrated supramolecular host–guest post-treatment strategy developed in this work. We used quasi-2D mixed chloride-bromide perovskites as the emissive layer, with *p*-fluorophenethylammonium bromide (p-F-PEABr) as the bulky spacer cation. 18-crown-6 molecules were introduced to suppress p-F-PEABr aggregation and inhibit the formation of low-dimensional phases.[25−27] The


https://doi.org/10.1021/acs.nanolett.5c06313
Nano Lett. XXXX, XXX, XXX−XXX

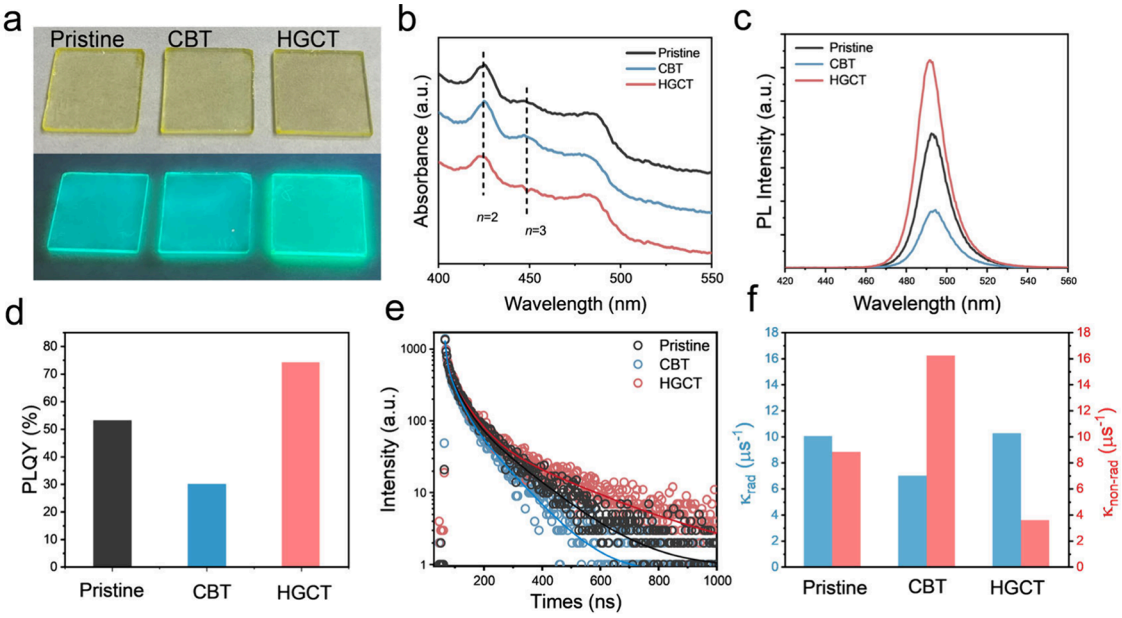


**Figure 2.** Optical properties of perovskite films with different treatments. a) Photographs of perovskite films under ambient light (top) and UV illumination (bottom). b) UV−vis absorption spectra, c) PL, d) PLQY, e) TRPL, and f) calculated radiative and nonradiative recombination ratios of pristine, CBT, and HGCT perovskite films.

device adopts a conventional p-i-n architecture, with sequentially deposited layers of PTAA/PVK/perovskite/PO-T2T/LiF/Al on an ITO substrate. To realize all-solution-processed PeLEDs, the small-molecule electron-transport material {2,4,6-tris[3-(diphenylphosphinyl)phenyl]-1,3,5-triazine} (PO-T2T) was dissolved in the nonpolar solvent CB. Although CB is widely used as an orthogonal solvent for 3D polycrystalline perovskite films, high-performance all-solution-processed PeLEDs based on quasi-2D perovskites are rarely reported, likely due to the adverse effects of CB on their luminescent properties. We therefore systematically investigated the interaction between CB and sky-blue quasi-2D perovskite films prior to all-solution-processed fabrication.

Quasi-2D perovskite grains are coated with bulky cations and 18-crown-6 molecules, which can be stripped by nonpolar processing solvents. Such solvent-induced removal of weakly bound organic components compromises their defect-passivation ability and degrades luminescence. To address the poor solubility of organic ammonium salts in nonpolar solvents, we designed a host−guest complexation system based on ion-dipole interactions between the bulky cations and the crown ether.[26,28] The cavity size of the crown ether is well-suited for selectively binding the ammonium group ($NH_3^+$) of primary amines through multiple N−H···O hydrogen bonds. This size-matched, high-affinity recognition enables stable and specific complexation with the $PEA^+$ moiety in p-F-PEABr. The resulting host−guest complex exhibits high solubility in CB, allowing mild nonpolar solvents to be used for perovskite surface post-treatment. This approach compensates for the solvent-induced loss of surface organic components during processing and preserves the structural integrity of the perovskite interface.

Figure 1b illustrates the proposed host−guest configuration between the crown ether (host) and p-F-PEABr (guest) molecules. To examine their interaction mechanism, we characterized the local chemical environment using $^{13}C$ nuclear magnetic resonance (NMR) spectroscopy. In the neat crown ether solution, ethylene oxide signals appear near 70.5 ppm (Figure 1c). The p-F-PEABr solution alone shows no observable aliphatic or p-F-$PEA^+$-related signals, which is consistent with its poor solubility in the nonpolar solvent used. Upon crown ether addition, however, new aliphatic signals emerge at 32.6 and 40.5 ppm (Figure 1d).[28] Furthermore, multiple distinct signals in the aromatic region (130−160 ppm), characteristic of the carbon nuclei in the para-substituted benzene ring, are clearly observed, indicating that p-F-$PEA^+$ is now solubilized.[29,30] Moreover, the ethylene oxide peak of the crown ether shifts from 70.5 to 69.8 ppm, providing additional evidence for specific host−guest interactions. These results indicate that the crown ether modulates the physicochemical behavior of the ammonium salt through a cooperative supramolecular effect. Visual inspection confirmed that 2 mg of p-F-PEABr (0−8 mg) was poorly soluble in 1 mL of CB, yielding a precipitate. In contrast, the addition of crown ether promoted complete dissolution, visually demonstrating the host−guest complexation (Figure S1).

Functional group variations were further analyzed using Fourier transform infrared (FTIR) spectra (Figure 1e). The pristine crown ether exhibits C−O−C stretching vibrations at ~1114 $cm^{-1}$ and ~1250 $cm^{-1}$, which disappear in the host−guest complex.[31] For p-F-$PEA^+$, benzene skeleton vibrations are observed at 1526 $cm^{-1}$ and 1605 $cm^{-1}$; upon complexation, these peaks shift and broaden, indicating altered molecular interactions.[32] Together, these findings confirm that the lipophilic crown ether significantly enhances the dispersibility of p-F-PEABr in low-polarity solvents.

We further investigated the effect of surface treatment using pure CB and CB doped with the host−guest complex on the chemical composition of perovskite films. X-ray photoelectron spectroscopy (XPS) results revealed that after spin-coating with pure CB, the ratios of halide/Pb, F/Pb, and O/Pb all decreased (Figure 1f−h and Figure S2), indicating that CB readily induces halide vacancy defects and leads to the removal of bulky cations and crown ether molecules from the emissive


https://doi.org/10.1021/acs.nanolett.5c06313
Nano Lett. XXXX, XXX, XXX−XXX

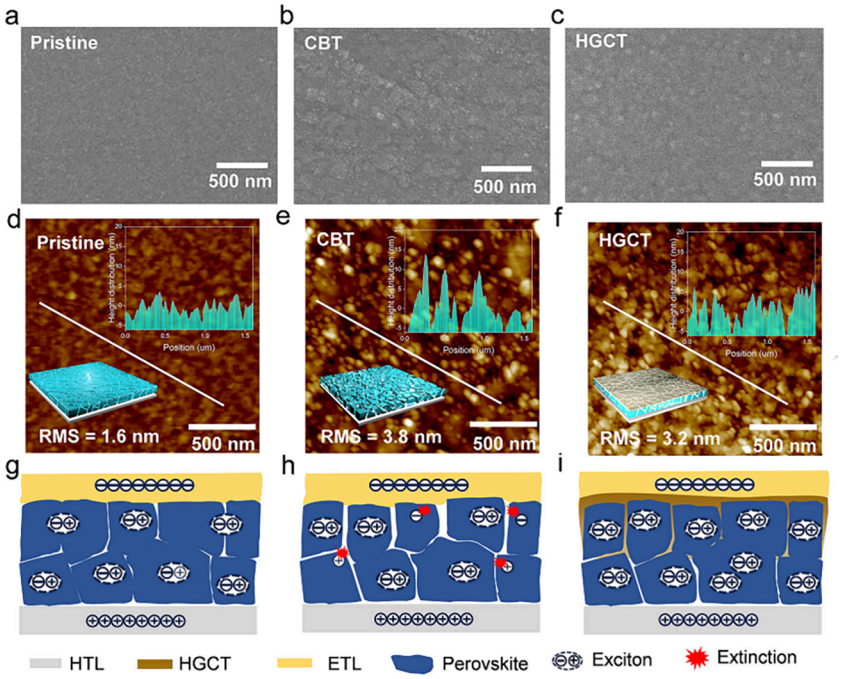


**Figure 3.** Morphological characterization and proposed operating mechanisms of perovskite films. a–c) SEM images, d–f) AFM images (including height profiles), and schematic cross-sectional illustrations of the pristine, CBT, and HGCT films, respectively. g–i) Corresponding schematic diagrams of the charge injection and recombination processes.

layer, which may account for the degradation in luminescence performance. In contrast, treatment with the host–guest complex-doped CB solution restored the halide/Pb and F/Pb ratios to levels close to those of the pristine film. Moreover, the O/Pb ratio increased significantly, likely due to the high concentration of crown ether in the solution. These results demonstrate that the host–guest complex-doped CB solution effectively compensates for the loss of organic components and halides caused by solvent processing, thereby mitigating the adverse effects of CB on the perovskite film.

For comparison, we prepared pristine, CB-treated ("CBT"), and host–guest complex-treated ("HGCT") perovskite films and evaluated their PL properties. We then evaluated the PL properties of pristine, CBT, and HGCT films. Under daylight, the CBT film shows no visible change relative to the pristine sample (Figure 2a). The absorption spectrum of the pristine film displays two distinct peaks at approximately 423 and 448 nm (Figure 2b), consistent with the reported $n = 2$ and $n = 3$ phases of quasi-2D perovskites.[13,14] The CB-treated film retains these low-dimensional phase signatures, and the spectral profile remains largely unchanged, indicating that the nonpolar CB solvent causes minimal morphological or absorption-related damage. However, PL spectra and PLQY measurements reveal a marked decline in luminescence after CB treatment: the PLQY drops from 53.2% to 30.1% (Figure 2c–d and Figure S3), likely due to surface damage and nonradiative defect formation. The HGCT film, however, exhibits significantly enhanced PL intensity and a PLQY of 74.2%, along with a reduced proportion of $n = 2$ and $n = 3$ phases. These results suggest that HGCT promotes secondary grain growth and phase redistribution, leading to improved luminescent properties.

Figure 2e presents the time-resolved photoluminescence (TRPL) decay curves of the pristine, CBT, and HGCT films, fitted using a triexponential function (fitting parameters in Table S1). The average PL lifetime ($\tau_{ave}$) decreases from 53.1 ns (pristine) to 43.1 ns after CB treatment, but increases to 72.4 ns for the HGCT film. From the PLQY and TRPL data, we calculated the radiative ($k_r$) and nonradiative ($k_{nr}$) recombination rates (Figure 2f). The CBT film increases $k_{nr}$ from 8.31 $\mu s^{-1}$ to 16.22 $\mu s^{-1}$ and slightly reduces $k_r$ from 10.03 $\mu s^{-1}$ to 6.98 $\mu s^{-1}$, whereas the HGCT film restores $k_r$ to near its initial value and strongly suppresses nonradiative recombination ($k_{nr} = 3.56$ $\mu s^{-1}$). These results indicate that the HGCT strategy enables effective defect passivation by filling vacancies and coordinatively unsaturated sites, thereby reducing nonradiative losses and enhancing radiative recombination.

The surface morphologies of the pristine, CBT, and HGCT films are compared in Figure 3a–c. A uniform and compact morphology is observed for the pristine film (Figure 3a). However, the CBT-processed film (Figure 3b) displays increased surface roughness and a distinct granular structure. This is attributed to partial dissolution of the film by the solvent, leading to poor grain connectivity. The HGCT approach effectively addresses this issue, yielding a film with significantly enhanced smoothness and continuity (Figure 3c). The modulating effect of the host–guest complex on film morphology was further investigated by atomic force microscopy (AFM, Figure 3d–f). The root-mean-square (RMS) roughness of the pristine perovskite film was only 1.6 nm, which increased to 3.8 nm after CB solvent washing, indicating the loss of surface components due to solvent treatment. Upon introduction of the host–guest complex, the film roughness decreased to 3.2 nm, and the height distribution histogram in the upper-right inset of the AFM image also confirmed improved film uniformity.

Figure 3g–i presents schematic diagrams illustrating the evolution of film morphology and defect states under pristine, CBT-, and HGCT-based conditions. The pristine film (Figure 3g) exhibits a compact, pinhole-free morphology, providing an


https://doi.org/10.1021/acs.nanolett.5c06313
Nano Lett. XXXX, XXX, XXX–XXX

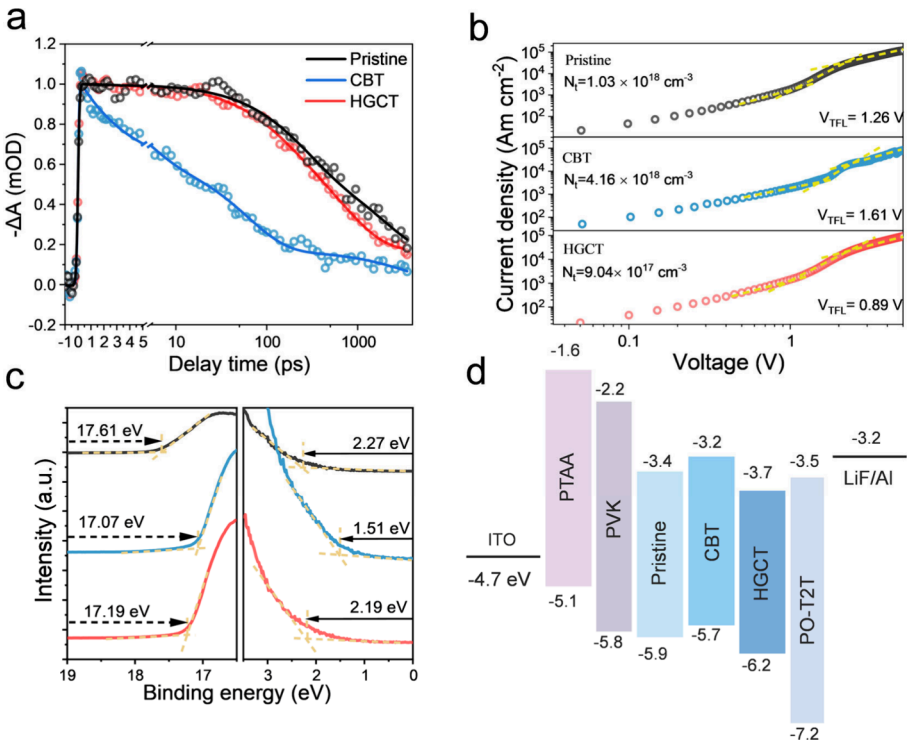


**Figure 4.** Photophysical properties and energy levels of the perovskite films. a) Normalized transient absorption kinetics probed at 485 nm for the pristine, CBT, and HGCT films. b) Current density−voltage (J-V) characteristics of hole-only devices (ITO/PEDOT:PSS/perovskite/$MoO_3$/Ag). c) Ultraviolet photoelectron spectroscopy spectra of the pristine, CBT, and HGCT films. d) Energy level diagram of the fabricated PeLEDs.

ideal environment for efficient exciton formation and radiative recombination. In contrast, the CBT film (Figure 3h) shows increased roughness and numerous grain boundaries, which introduce structural defects that impede charge transport and enhance nonradiative recombination. After treatment with the host−guest complex (Figure 3i), bulky cations permeate the perovskite surface and fill halogen vacancies, while crown ether molecules interact with undercoordinated lead ions, further passivating surface defects, as illustrated in Figure 3e. Furthermore, as shown in Figure S4, XRD patterns confirm that solvent washing reduces diffraction peak intensity, indicating degraded crystallinity, whereas the HGCT film exhibits stronger peaks, suggesting that the treatment promotes secondary crystallization and guides highly ordered crystal growth, resulting in a more structurally complete film with fewer defects.

To investigate how different treatment strategies influence carrier dynamics, we conducted femtosecond transient absorption (fs-TA) measurements on the perovskite films using a 365 nm excitation pulse.[33] The resulting TA spectral color maps and spectra for the pristine, CBT-, and HGCT-films are presented in Figure S5. All samples exhibited a dominant negative photobleaching (PB) signal, indicative of a state-filling effect, accompanied by two weaker photoinduced absorption peaks. We further analyzed the exciton recombination dynamics by fitting the normalized PB decay kinetics with a triexponential fitting (Figure 4a). The three components correspond to distinct processes: a subpicosecond component (I) associated with carrier capture by shallow traps, a picosecond component (II) attributed to deep traps, and a nanosecond component (III) representing radiative exciton recombination.[34] Analysis of the TA decay components reveals a clear trend (Table S2). Compared to the pristine sample, the CBT sample shows a marked increase in the proportion of the two faster decay components ($\tau_1$ and $\tau_2$), indicating a higher density of trap states likely exposed during solvent washing. In contrast, the HGCT film exhibits a substantial increase in the relative amplitude of the slowest, nanosecond-scale component ($\tau_3$), restoring it to a level comparable to the pristine film. This shift confirms that the host−guest complex treatment effectively passivates trap sites, suppressing nonradiative recombination and promoting radiative exciton radiative recombination.

To quantify the defect state density in the perovskite films, we performed space-charge-limited current (SCLC) measurements on hole-only devices with the structure ITO/PEDOT:PSS/perovskite/$MoO_3$/Ag (Figure 4b). The current density−voltage (J-V) curves show three characteristic regions: Ohmic, trap-filled limit (TFL), and Child's law regimes. The trap-filled limit voltage ($V_{TFL}$) was determined to be 1.28 V for the pristine film, 1.68 V for the CBT film, and 0.89 V for the HGCT film. The trap density ($n_{trap}$) was calculated using the equation:

$$n_{trap} = \frac{2\varepsilon_0 \varepsilon V_{TFL}}{eL^2}$$

where $\varepsilon_0$ is the vacuum permittivity, $\varepsilon_r$ is the relative permittivity of the perovskite, e is the elementary charge, and $L$ is the film thickness of the perovskite. The calculated trap densities are $1.03 \times 10^{16}$ $cm^{-3}$ for the pristine film, $4.16 \times 10^{16}$ $cm^{-3}$ for the CBT film, and $9.04 \times 10^{15}$ $cm^{-3}$ for the HGCT film. This trend demonstrates that the host−guest complexation treatment effectively passivates traps, which is expected to suppress nonradiative recombination and prolong charge carrier lifetime, a key factor in enhancing device performance.


https://doi.org/10.1021/acs.nanolett.5c06313
Nano Lett. XXXX, XXX, XXX−XXX

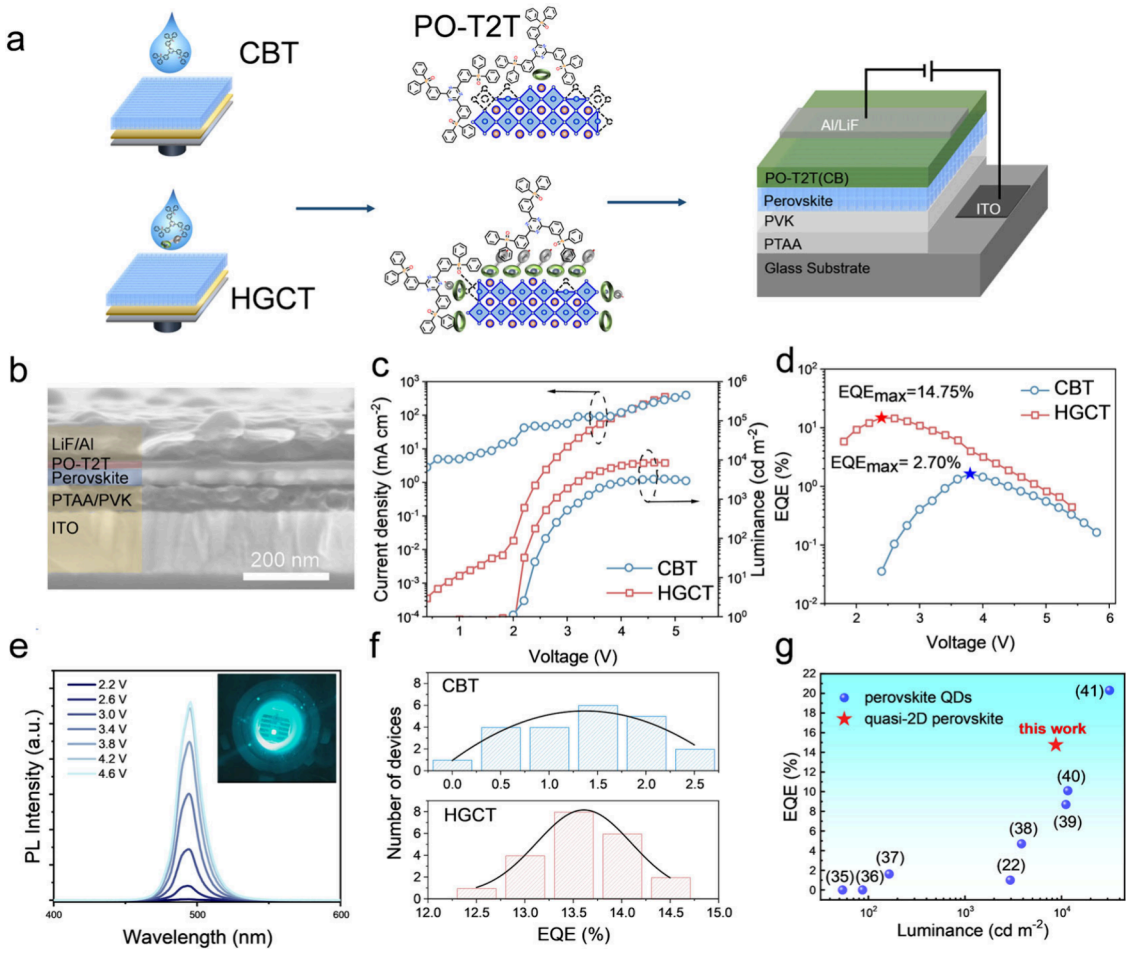


**Figure 5.** Device performance of all-solution-processed sky-blue PeLEDs. a) Schematic of the all-solution-processed sky-blue PeLEDs. b) Cross-section SEM image of the device. c) Current density-luminance−voltage (J-L-V) curves and d) external quantum efficiency-voltage (EQE-V) characteristics. e) Electroluminescence (EL) spectra of the optimized device; inset shows a photograph of the operating device at 4.2 V. f) Statistical distribution of EQE values across multiple devices. g) Comparison of EQE versus luminance for our device and other reported blue PeLEDs.

We employed ultraviolet photoelectron spectroscopy (UPS) to determine the energy levels of the pristine, CBT, and HGCT perovskite films. The secondary electron cutoff and onset regions are shown in Figure 4c. The pristine film has a valence band maximum (VBM) of −5.9 eV and a conduction band minimum (CBM) of −3.4 eV. After CB treatment, the CBT film exhibits an upward shift in both energy levels: the VBM increases to −5.7 eV and the CBM to −3.2 eV (Figure 4d). This shift reduces the injection barriers for holes while increasing the injection barriers for electrons. In contrast, the HGCT film shows an overall downward shift, with the VBM and CBM moving to −6.2 eV and −3.7 eV, respectively. Although this slightly increases the hole injection barrier relative to the HTL, the CBM of the HGCT film aligns more closely with the LUMO of the PO-T2T ETL (−3.5 eV), resulting in a lower electron injection barrier. It should be noted that the post-treatment with solvent is also accompanied by the generation of defect states, which can consequently affect the efficiency of carrier injection and recombination. Therefore, its ultimate impact must be further verified in actual devices.

The preceding results demonstrate that the HGCT effectively regulates the optical properties, crystallization behavior, and surface morphology of the perovskite films. Previous studies indicate that solution-processed PO-T2T can modify the perovskite/ETL interface, with its P═O groups passivating undercoordinated lead defects and improving electron injection. However, in our all-solution-processed approach, both the host−guest complex and PO-T2T are dissolved in CB, resulting in coupled effects. To isolate the specific contribution of PO-T2T, we fabricated the PO-T2T ETL by thermal evaporation and systematically evaluated the influence of different post-treatment processes on the perovskite film and device performance (Figure S6a).

The PeLEDs featured a layered structure of ITO/PTAA/PVK/perovskite/PO-T2T/LiF/Al, with the ETL and LiF/Al cathode deposited by thermal evaporation (see Experimental Section). Current density−voltage (J-V) measurements show that the pristine device exhibits a very low leakage current ($10^{-5}$-$10^{-4}$ mA cm$^{-2}$) (Figure S6b), consistent with the compact, pinhole-free perovskite morphology observed by SEM. CB treatment significantly increases leakage current, indicating solvent-induced film degradation. In contrast, the HGCT-based device shows substantially reduced leakage, suggesting that the host−guest complex forms a passivating layer that prevents direct interlayer contact.

The pristine device, with its intact emissive layer, achieves efficient charge injection and radiative recombination, yielding


https://doi.org/10.1021/acs.nanolett.5c06313
Nano Lett. XXXX, XXX, XXX−XXX

a peak EQE of 12.97% and a maximum luminance of 8146 cd $m^{-2}$ (Figure S6c,d). CB treatment exposes lead sites and halogen vacancies, creating leakage pathways that degrade performance: the maximum EQE falls below 2% and luminance drops to 3581 cd $m^{-2}$. After HGCT treatment, defect passivation and vacancy replenishment restore performance, with a peak EQE exceeding 10.51% and a maximum luminance of 12476 cd $m^{-2}$. Statistical analysis over 15 devices confirms an average EQE improvement from 0.63% to 9.44%, a nearly 15-fold enhancement (Figure S6e).

We then integrated the host−guest complex with PO-T2T to enable simultaneous perovskite surface repair and ETL deposition in a one-step spin-coating method. Figure 5a illustrates the fabrication of all-solution-processed sky-blue PeLEDs using PO-T2T blended with either CBT- or HGCT-based perovskite. The HIL stack and ETL annealing temperature were also optimized, as detailed in Figures S7, S8 and Table S3. Cross-sectional SEM images show a uniform, ∼40 nm thick PO-T2T layer atop the perovskite (Figure 5b). The CBT-based device exhibits severe leakage current (Figure 5c), limiting performance to a maximum luminance of 3284 cd $m^{-2}$ and a peak EQE of 2.7%. In contrast, the HGCT-based device shows significantly suppressed leakage, attributable to surface passivation and structural reconstruction of the perovskite. This yields a low turn-on voltage of 2.0 V, a maximum luminance of 8740 cd $m^{-2}$, and a peak EQE of 14.75%—corresponding to 2.7- and 5.5-fold improvements in brightness and EQE, respectively, over the CBT device (Figure 5d).

We examined the effect of separately adding f-F-PEABr or 18-crow-6 alone to the solution-processed ETL. Due to the low solubility of f-F-PEABr in CB, the solution was filtered prior to use. As shown in Figure S9 and Table S4, even trace dissolved f-F-PEABr increased the EQE by approximately 2-fold relative to the pristine device, confirming that CB partially dissolves organic bulky ligands during spin-coating. Adding only crown ether yielded a more pronounced improvement in both efficiency and brightness, likely because of its higher solubility in CB, which more effectively replenishes the organic additive. Together, these results demonstrate that the HGCT strategy can compensate for solvent-induced loss of functional components during ETL processing, leading to an overall enhancement in device performance.

The HGCT device exhibits stable sky-blue electroluminescence centered at 495 nm, with a narrow fwhm of 15.8 nm and negligible spectral shift under increasing voltage (Figure 5e). The inset shows uniform emission at 4.2 V. Performance statistics over 20 devices confirm high reproducibility, with an average EQE of 13.59 ± 1.16% (Figure 5f). A comparison with reported sky-blue PeLEDs (Figure 5g) shows that high-performance devices are predominantly quantum-dot-based.[35−41] Our all-solution-processed quasi-2D PeLED achieves a record EQE for such systems, providing an important reference for the development of thin-film blue PeLEDs (Table S5).

In summary, we have developed a supramolecular strategy for fabricating all-solution-processed PeLEDs. This approach utilizes host−guest complexation between crown ether and ammonium salt molecules to enable the dissolution of p-PEABr in nonpolar solvents. The resulting host−guest complex treatment effectively mitigates solvent-induced damage to the underlying emissive layer during solution processing, facilitating the deposition of a smooth, dense ETL. Moreover, the introduced crown ether and p-PEABr compensate for the loss of organic ligands and additives during fabrication, passivating surface defects and reducing trap-assisted nonradiative recombination. These improvements lead to a significant enhancement in luminescence efficiency and device performance. We achieved an average EQE of 13.59 ± 1.16% across more than 20 devices, with a peak EQE of 14.75% and a maximum luminance of 8740 cd $m^{-2}$. This supramolecular approach offers a promising route to high-performance, all-solution-processed perovskite optoelectronic devices.

## ■ ASSOCIATED CONTENT

### Supporting Information

The Supporting Information is available free of charge at https://pubs.acs.org/doi/10.1021/acs.nanolett.5c06313.

Detailed additional experimental data including material, methods, and characterization details; XPS, PLQY, and TA spectra; XRD patterns; J-V, L-V, and EQE-V curves of PeLEDs (PDF)

## ■ AUTHOR INFORMATION


### Corresponding Authors

**Zhibin Wang** − *College of Physics and Energy, Fujian Normal University, Fuzhou, Fujian 350117, P. R. China*; Email: zhibinwang@fjnu.edu.cn

**Daqin Chen** − *College of Physics and Energy, Fujian Normal University, Fuzhou, Fujian 350117, P. R. China; Fujian Provincial Engineering Technology Research Center of Solar Energy Conversion and Energy Storage, Fujian Normal University, Fuzhou, Fujian 350117, P. R. China*; orcid.org/0000-0003-0088-2480; Email: dqchen@fjnu.edu.cn

### Authors

**Naizhong Jiang** − *College of Physics and Energy, Fujian Normal University, Fuzhou, Fujian 350117, P. R. China*

**Song Zheng** − *College of Physics and Energy, Fujian Normal University, Fuzhou, Fujian 350117, P. R. China*

**Zhehong Zhou** − *College of Physics and Energy, Fujian Normal University, Fuzhou, Fujian 350117, P. R. China*

**Ruidan Zhang** − *College of Physics and Energy, Fujian Normal University, Fuzhou, Fujian 350117, P. R. China*; orcid.org/0000-0002-9582-1869

**Lingwei Zeng** − *School of Chemistry and Chemical Engineering, Key Laboratory of Theoretical Organic Chemistry and Functional Molecule of Ministry of Education, Hunan University of Science and Technology, Xiangtan, Hunan 411201, P. R. China*

**Feng Huang** − *College of Physics and Energy, Fujian Normal University, Fuzhou, Fujian 350117, P. R. China*

Complete contact information is available at: https://pubs.acs.org/10.1021/acs.nanolett.5c06313


### Notes

The authors declare no competing financial interest.

## ■ ACKNOWLEDGMENTS

This research was supported by the National Natural Science Foundation of China (52572155, 52102159, and 52272141) and the Natural Science Foundation of Fujian Province (2024J02014 and 2025J01655).

## REFERENCES


(1) Dutta, A.; Behera, R. K.; Pal, P.; Baitalik, S.; Pradhan, N. Near-unity photoluminescence quantum efficiency for all $CsPbX_3$ (x = Cl, Br, and I) perovskite nanocrystals: a generic synthesis approach. *Angew. Chem., Int. Ed.* **2019**, *58* (17), 5552−5556.

(2) Yu, D.; Cao, F.; Gao, Y.; Xiong, Y.; Zeng, H. Room-temperature ion-exchange-mediated self-assembly toward formamidinium perovskite nanoplates with finely tunable, ultrapure green emissions for achieving Rec. 2020 displays. *Adv. Funct. Mater.* **2018**, *28* (19), 1800248.

(3) Luo, J.; Wang, X.; Li, S.; Liu, J.; Guo, Y.; Niu, G.; Yao, L.; Fu, Y.; Gao, L.; et al. Efficient and stable emission of warm-white light from lead-free halide double perovskites. *Nature* **2018**, *563* (7732), 541−545.

(4) Kim, J. S.; Heo, J.-M.; Park, G.-S.; Woo, S.-J.; Cho, C.; Yun, H. J.; Kim, D.-H.; Park, J.; Lee, S.-C.; Park, S.-H.; Yoon, E.; Greenham, N. C.; Lee, T.-W. Ultra-bright, efficient and stable perovskite light-emitting diodes. *Nature* **2022**, *611* (7937), 688−694.

(5) Zheng, S.; Wang, Z.; Jiang, N.; Huang, H.; Wu, X.; Li, D.; Teng, Q.; Li, J.; Li, C.; Li, J.; Pang, T.; Zeng, L.; Zhang, R.; Huang, F.; Lei, L.; Wu, T.; Yuan, F.; Chen, D. Ultralow-voltage-driven efficient and stable perovskite light-emitting diodes. *Sci. Adv.* **2024**, *10* (36), 167211.

(6) Tan, Z.-K.; Moghaddam, R. S.; Lai, M. L.; Docampo, P.; Higler, R.; Deschler, F.; Price, M.; Sadhanala, A.; Pazos, L. M.; et al. Bright light-emitting diodes based on organometal halide perovskite. *Nat. Nanotechnol.* **2014**, *9* (9), 687−692.

(7) Feng, S.-C.; Shen, Y.; Hu, X.-M.; Su, Z.-H.; Zhang, K.; Wang, B.-F.; Cao, L.-X.; Xie, F.-M.; Li, H.-Z.; Gao, X.; Tang, J.-X.; Li, Y.-Q. Efficient and stable red perovskite light-emitting diodes via thermodynamic crystallization control. *Sci. Adv.* **2024**, *36* (44), 2410255.

(8) Bai, W.; Xuan, T.; Zhao, H.; Dong, H.; Cheng, X.; Wang, L.; Xie, R. J. Perovskite light-emitting diodes with an external quantum efficiency exceeding 30%. *Adv. Mater.* **2023**, *35* (39), 2302283.

(9) Chen, B.; Liu, H.; Yang, J.; Ahmadi, M.; Chen, Q.; Yin, N.; Zhang, S.; Xiao, M.; Zhang, H.; Xu, L.; Chen, P. Coordination of thermally activated delayed fluorescent molecules for efficient and stable perovskite light-emitting diodes. *Adv. Funct. Mater.* **2024**, *34* (38), 2402522.

(10) Farooq, M. U.; Khan, M.; Faraz, A.; Maqsood, A.; Ahmad, W.; Li, L. Comparative study of ZnTe thin films prepared using close space sublimation (CSS) and electron beam evaporation (EBE) thin film fabrication techniques for optoelectronic applications. *Mater. Technol.* **2014**, *29* (1), 29−35.

(11) Vaynzof, Y. The future of perovskite photovoltaics-thermal evaporation or solution processing? *Adv. Energy Mater.* **2020**, *10* (48), 2003073.

(12) Guo, K.; Li, N.; Zhang, M.; Ren, L.; Qiao, F.; Pan, S.; Wang, X.; Yuan, F.; Zhang, F. Efficient all-solution-processed perovskite light-emitting diodes via a room-temperature vapor-treated interlayer. *ACS Appl. Mater. Interfaces* **2025**, *17*, 15688−15697.

(13) Xiao, M.; Yang, J.; Zhang, W.; Xu, L.; Zhang, J.; Li, W.; Chen, C.; Zhou, T.; Zhang, H.; Chen, B.; et al. Coherence programming for efficient linearly polarized perovskite light-emitting diodes. *ACS Nano* **2024**, *18* (42), 29261−29272.

(14) Xiang, T.; Li, T.; Wang, M.; Zhang, W.; Ahmadi, M.; Wu, X.; Xu, T.; Xiao, M.; Xu, L.; Chen, P. 12-Crown-4 ether assisted in-situ grown perovskite crystals for ambient stable light emitting diodes. *Nano Energy* **2022**, *95*, 107000.

(15) Chen, R.; Wang, Z.; Pang, T.; Teng, Q.; Li, C.; Jiang, N.; Zheng, S.; Zhang, R.; Zheng, Y.; Chen, D.; Yuan, F. Ultra-narrow-bandwidth deep-red electroluminescence based on green plant-derived carbon dots. *Adv. Mater.* **2023**, *35* (36), 2302275.

(16) Li, D.; Wang, Z.; Zheng, S.; Jiang, N.; Feng, C.; Wu, X.; Huang, H.; Pang, T.; Zeng, L.; Zhang, R.; Huang, F.; Chen, D. Full-spectrum carbon dots electroluminescent white light-emitting diodes with a record color rendering index of 94. *Adv. Funct. Mater.* **2025**, *35* (28), 2424929.

(17) Zhu, H.; Tong, G.; Li, J.; Tao, X.; Shen, Y.; Sheng, Y.; Shi, L.; Xie, F.; Tang, J.; et al. Acid-etching induced metal cation competitive lattice occupancy of perovskite quantum dots for efficient pure-blue QLEDs. *Interdiscip. Mater.* **2024**, *3* (3), 437−447.

(18) Wu, M.; Zhao, D.; Wang, Z.; Yu, J. High-luminance perovskite light-emitting diodes with high-polarity alcohol solvent treating PEDOT:PSS as hole transport layer. *Nanoscale Res. Lett.* **2018**, *13* (1), 128−137.

(19) Zhang, C.; Wang, B.; Zheng, W.; Huang, S.; Kong, L.; Li, Z.; He, G.; Li, L. Hydrofluoroethers as orthogonal solvents for all-solution processed perovskite quantum-dot light-emitting diodes. *Nano Energy* **2018**, *51*, 358−365.

(20) Jo, C.-S.; Noh, K.; Noh, S. H.; Yoo, H.; Kim, Y.; Jang, J.; Lee, H. H.; Jung, Y.-J.; Lee, J.-H.; et al. Solution-processed fabrication of light-emitting diodes using $CsPbBr_3$ perovskite nanocrystals. *ACS Appl. Nano Mater.* **2020**, *3* (12), 11801−11810.

(21) Shi, X.; Zhang, J.; Kong, L.; Wang, L.; Dou, Y.; Wang, S.; Li, W.; Zhang, X.; Yan, L.; et al. A mixed solvent strategy enabling efficient all-solution-processed perovskite light-emitting diodes. *J. Mater. Chem. C* **2022**, *10* (23), 8964−8971.

(22) Zhang, M.; Bi, C.; Xia, Y.; Sun, X.; Wang, X.; Liu, A.; Tian, S.; Liu, X.; de Leeuw, N. H.; Tian, J. Water-driven synthesis of deep-blue perovskite colloidal quantum wells for electroluminescent devices. *Angew. Chem., Int. Ed.* **2023**, *62* (12), No. e202300149.

(23) Liu, A.; Bi, C.; Tian, J. All solution-processed high-performance pure-blue perovskite quantum-dot light-emitting diodes. *Adv. Funct. Mater.* **2022**, *32* (44), 2207069.

(24) Jiang, N.; Wang, Z.; Zheng, Y.; Guo, Q.; Niu, W.; Zhang, R.; Huang, F.; Chen, D. 2D/3D heterojunction perovskite light-emitting diodes with tunable ultrapure blue emissions. *Nano Energy* **2022**, *97* (15), 107181.

(25) Landini, D.; Maia, A.; Montanari, F.; Pirisi, F. M. Crown ethers as phase-transfer catalysts. A comparison of anionic activation in aqueous-organic two-phase systems and in low polarity anhydrous solutions by perhydrodibenzo-18-crown-6, lipophilic quaternary salts, and cryptands. *J. Chem. Soc., Perkin Trans. 2* **1980**, No. 1, 46−51.

(26) Zhang, H.; Eickemeyer, F. T.; Zhou, Z.; Mladenovic, M.; Jahanbakhshi, F.; Merten, L.; Hinderhofer, A.; Hope, M. A.; Ouellette, O.; Mishra, A.; Ahlawat, P.; Ren, D.; Su, T.-S.; Krishna, A.; Wang, Z.; Dong, Z.; Guo, J.; Zakeeruddin, S. M.; Schreiber, F.; Hagfeldt, A.; Emsley, L.; Rothlisberger, U.; Milic, J. V.; Gratzel, M. Multimodal host-guest complexation for efficient and stable perovskite photovoltaics. *Nat. Commun.* **2021**, *12* (1), 3383.

(27) Zheng, S.; Wang, Z.; Zheng, G.; Huang, H.; Jiang, N.; Zhou, Z.; Wu, X.; Pang, T.; Zeng, L.; Zhang, R.; Huang, F.; Chen, D. Stable sky-blue perovskite LEDs achieved by efficient sub-bandgap emission with 24.5% PCE. *Adv. Funct. Mater.* **2025**, e21079.

(28) Zhao, C.; Zhou, Z.; Almalki, M.; Hope, M. A.; Zhao, J.; Gallet, T.; Krishna, A.; Mishra, A.; Eickemeyer, F. T.; Xu, J.; Yang, Y.; Zakeeruddin, S. M.; Redinger, A.; Savenije, T. J.; Emsley, L.; Yao, J.; Zhang, H.; Gratzel, M. Stabilization of highly efficient perovskite solar cells with a tailored supramolecular interface. *Nat. Commun.* **2024**, *15* (1), 7139.

(29) Viesser, R. V.; Ducati, L. C.; Tormena, C. F.; Autschbach, J. The unexpected roles of $\sigma$ and $\pi$ orbitals in electron donor and acceptor group effects on the 13C NMR chemical shifts in substituted benzenes. *Chem. Sci.* **2017**, *8* (9), 6570−6576.

(30) Viesser, R. V.; Ducati, L. C.; Tormena, C. F.; Autschbach, J. The halogen effect on the $^{13}C$ NMR chemical shift in substituted benzenes. *Phys. Chem. Chem. Phys.* **2018**, *20* (16), 11247−11259.

(31) Wang, W.; Peng, X.; Zhang, J.; Huang, R.; Guo, H.; Pan, Z.; Rao, H.; Zhong, X.; Zhang, G. Crown ether-modified 1D/3D heterojunction for efficient and stable carbon-based $CsPbI_3$ perovskite solar cells. *ACS Appl. Mater. Interfaces* **2024**, *16* (49), 67752−67760.

(32) Zhu, S.; Wu, J.; Sun, W.; Pan, W.; Cai, F.; Liu, J.; Chen, L.; Chen, X.; Wang, C.; et al. Interlayer modification using phenylethylamine tetrafluoroborate for highly effective perovskite solar cells. *ACS Appl. Energy Mater.* **2022**, *5* (1), 658−666.




https://doi.org/10.1021/acs.nanolett.5c06313
Nano Lett. XXXX, XXX, XXX−XXX

(33) Zhang, R.; Zhou, Z.; Li, X.; Pang, T.; Song, T.; Wu, H.; Liao, Q.; Wang, Z.; Huang, F.; et al. Low-threshold and ultrastable amplified spontaneous emission from $CsPbBr_3$@glass via glass network modulation. *ACS Nano* **2025**, *19* (14), 14318−14329.
(34) Wang, Z.; Zheng, S.; Jiang, N.; Huang, H.; Wu, X.; Zhang, R.; Lin, Y.; Lin, L.; Zhou, X.; Zeng, R.; Pang, T.; Wu, T.; Huang, F.; Chen, D. Minimizing interfacial energy losses with carbon dot bifacial modification layers for high-efficiency and stable perovskite LEDs. *Adv. Funct. Mater.* **2025**, *35* (28), 2423608.
(35) Wei, Y.; Li, X.; Chen, Y.; Cheng, Z.; Xiao, H.; Li, X.; Ding, J.; Lin, J. In situ light-initiated ligands cross-linking enables efficient all-solution-processed perovskite light-emitting diodes. *J. Phys. Chem. Lett.* **2020**, *11* (3), 1154−1161.
(36) Li, G.; Rivarola, F. W. R.; Davis, N. J.; Bai, S.; Jellicoe, T. C.; de la Peña, F.; Hou, S.; Ducati, C.; Gao, F.; et al. Highly efficient perovskite nanocrystal light-emitting diodes enabled by a universal crosslinking method. *Adv. Mater.* **2016**, *28* (18), 3528.
(37) Sun, Y.; Yang, X.; Jiao, W.; Wu, J.; Zhao, Z. All-inorganic perovskite quantum dots based on $InX_3$-trioctylphosphine oxide hybrid passivation strategies for high-performance and full-colored light-emitting diodes. *ACS Appl. Electron. Mater.* **2021**, *3* (1), 415−421.
(38) Bi, C.; Yao, Z.; Sun, X.; Wei, X.; Wang, J.; Tian, J. Perovskite quantum dots with ultralow trap density by acid etching-driven ligand exchange for high luminance and stable pure-blue light-emitting diodes. *Adv. Mater.* **2021**, *33* (15), 2170119.
(39) Liu, A.; Bi, C.; Tian, J. All solution-processed high-performance pure-blue perovskite quantum-dot light-emitting diodes. *Adv. Funct. Mater.* **2022**, *32* (44), 2207069.
(40) Liu, A.; Bi, C.; Li, J.; Zhang, M.; Cheng, C.; Binks, D.; Tian, J. High color-purity and efficient pure-blue perovskite light-emitting diodes based on strongly confined monodispersed quantum dots. *Nano Lett.* **2023**, *23* (6), 2405−2411.
(41) Yao, Z.; Bi, C.; Xu, R.; Zhang, X.; Qian, L.; Xiang, C. Decoupling the exciton-carrier interaction for highly efficient pure blue perovskite light-emitting diodes exceeding 20%. *Adv. Mater.* **2025**, *37* (42), No. e20131.


https://doi.org/10.1021/acs.nanolett.5c06313
*Nano Lett.* XXXX, XXX, XXX−XXX